


Diffusion tensor subspace imaging of double diffusion-encoded MRI delineates small fibers and gray-matter microstructure not visible with single encoding techniques

Elizabeth B. Hutchinson¹  | Jean-Philippe Galons² | Courtney J. Comrie¹ | Thomas G. Beach³ | Geidy E. Serrano³ | Mark W. Bondi⁴ | Seraphina K. Solders⁵ | Vitaly L. Galinsky^{5,6} | Lawrence R. Frank^{5,7,8}

Correspondence

Elizabeth B. Hutchinson, 1230 N. Cherry Ave., Biosciences Research Laboratory, Rm 164, Tucson, AZ 85721, USA.
Email: hutchinsone@arizona.edu

Funding information

National Institute on Aging (NIA)/National Institutes of Health (NIH), Grant/Award Numbers: R03AG071903, R01AG079280; National Institutes of Health, Grant/Award Number: S10 OD025016; National Institute of Neurological Disorders and Stroke, Grant/Award Number: U24 NS072026; the NIA, Grant/Award Numbers: P30 AG19610, P30AG072980; Arizona Department of Health Services, Grant/Award Number: 211002; Arizona Biomedical Research Commission, Grant/Award Numbers: 4001, 0011, 05-901, 1001; The Michael J. Fox Foundation for Parkinson's Research

Abstract

Purpose: Double diffusion encoding (DDE) acquisition strategies promise specificity for small-dimensional structures inaccessible to single diffusion encoding (SDE). For DDE-weighted MRI scans to become relevant for whole brain imaging, signal reconstruction frameworks must accurately report microstructural features of interest—especially microscale anisotropy in complex tissue environments. This study examined the recently developed diffusion tensor subspace imaging (DiTSI) framework and its radial and spherical anisotropy metrics (RA and SA, respectively) in postmortem human brain tissue specimens.

Methods: MRI microscopy including multishell SDE-weighted and DDE-weighted imaging was performed for healthy brain stem and temporal lobe specimens and for specimens with Alzheimer's disease pathology and neurodegeneration. The DiTSI framework was compared with four other diffusion MRI frameworks, and angular and radial DDE sampling were evaluated.

Results: DDE acquisition and the DiTSI metric maps of SA and RA in temporal lobe and brain-stem specimens were found to be distinct from fractional anisotropy and orientation dispersion index in providing complementary and selective contrast of microscale anisotropy at the gray-matter/white-matter interface in the cortex and in hippocampal layers. DiTSI maps also unmasked small fascicles in the brain stem that were not detectable by SDE techniques and provided selective contrast across the major fiber pathways. Results also revealed prominent reductions of SA and RA in tissue with Alzheimer's disease pathology that were not observed for any other framework.

Conclusions: New contrasts were evident for DiTSI framework metrics over a range of tissue environments with promise toward providing novel markers of pathology.

KEYWORDS

brain stem, diffusion tensor subspace imaging, double diffusion encoding, microscale anisotropy, temporal lobe

For affiliations refer to page 2383

This is an open access article under the terms of the [Creative Commons Attribution-NonCommercial](https://creativecommons.org/licenses/by-nc/4.0/) License, which permits use, distribution and reproduction in any medium, provided the original work is properly cited and is not used for commercial purposes.

© 2025 The Author(s). *Magnetic Resonance in Medicine* published by Wiley Periodicals LLC on behalf of International Society for Magnetic Resonance in Medicine.

1 | INTRODUCTION

Measurement of specific microscale cellular features within complex tissue environments across brain structures is a major goal for diffusion MRI (dMRI) techniques to enable specific detection of pathologies^{1–3} and to improve the accuracy of biophysical models such as fiber tractography.^{4–6} Single-diffusion encoding (SDE) acquisition strategies⁷ are by far the most commonly used, as they are easily implemented and can support a wide range of measurement and modeling techniques from diffusion tensor imaging (DTI)⁸ to more sophisticated non-Gaussian frameworks^{9,10} or biophysical models of neurites¹¹ and fiber tracts.¹² Although SDE methods are very effective for characterization of simple tissue geometries such as coherent white matter (WM), they are inherently limited in their ability to measure specific cellular features within complex tissues such as WM fibers traversing complex tissue environments, organization of neurites in gray matter (GM), or subvoxel multifiber organization.

Double diffusion encoding (DDE) strategies,^{13–17} in which two sets of pulsed field gradients (PFGs) are varied in amplitude and direction relative to one another within a single acquisition period, result in intrinsic sensitivity to specific dimensional features, especially restricted pores of different volume or length scales and microscale geometry, especially microscale anisotropy (μA). This strategy of probing microscale features using a highly selective DDE acquisition is conceptually appealing for designing new contrasts for brain tissue and pathology, but unfortunately the complicated gradient encoding translates into a much more complicated analysis problem of relating the signal variations to structural and physiological characteristics of the tissues. Although significant recent work has been done to make DDE clinically feasible,^{18–21} no agreed-upon optimal approach has been identified that is sensitive to the complexities of tissue microstructure across the whole brain.

To address this problem, the new technique of diffusion tensor subspace imaging (DiTSI)⁵ was developed to characterize μA in tissues for which analytical models are insufficient. The DiTSI framework is conceptually grounded by a subspace representation of the DDE signal, in which angular and radial dependencies are separable and can be flexibly reported by summary metrics that are defined over different length scale and angular limits. The DDE encoding to support this framework is similarly based on a subspace structure in which b-vector pairs for the two DDE PFG blocks have identical orientations and are collected over a range of b_1 and b_2 weights. The mathematical details of this method are described more completely in an earlier publication⁵ and are summarized in Section 2. Ultimately, the rich and high-dimensional

representation of the DDE signal by DiTSI can be used to generate scalar maps that selectively probe different length scale and shape regimes in complex tissue environments. The general DiTSI reconstruction algorithm enables any selection of angular or length-scale limits to specify higher order tensor characterizations of the tissue–signal relationships. For this study, we examine two new scalar metrics, the spherical anisotropy (SA) and the radial anisotropy (RA), which have been formulated to reduce the high-dimensional signal to more easily interpretable scalars that are sensitive to microscale anisotropy. These metrics arise from the separability of angular and radial variance in the DiTSI representation of the spin density function (Φ) such that SA reports angular variations of Φ over all radial dependencies, and RA reports radial variations over all angular dependencies. Although recent simulation studies in human brain imaging⁵ and muscle tissue experiments²² all support the feasibility and promise of the DiTSI framework, a more rigorous evaluation of DiTSI metrics to discern cellular features in brain tissue is needed to enable interpretation of these maps and to guide the development of future DiTSI scalar metrics for practical utility in clinical settings, particularly in conditions such as Alzheimer's disease (AD), in which the detection of subtle but complex changes in tissue microstructure is paramount.

The objectives of the present study are to rigorously evaluate DiTSI representation of DDE data for sensitivity and specificity of the SA and RA metrics to microscale features across a range of complexity, from single fiber coherent WM to mixed composition GM, and to evaluate the dependence of these metrics on radial and angular diffusion-encoding sampling. Postmortem tissue from the brain stem and temporal lobe were selected for this study, as each includes a range of complexity in fiber architecture and GM microstructure. DDE data in these specimens and in an additional specimen with AD pathology were collected with a comprehensive sampling scheme and compared with SDE methods to determine the comparative representation of microstructural information across dMRI methods.

2 | THEORY

The DiTSI framework originates from the conjugate relationship between the measured DDE signal $W(r, q_1, q_2)$ and the spin density function $\Phi(r, R_1, R_2)$ at each voxel coordinate, r , where q_1 and q_2 are q -space values (i.e., $\mathbf{q} = \gamma \mathbf{G} \delta$, where γ is the gyromagnetic ratio; \mathbf{G} is the gradient vector; δ is the gradient duration of each PFG block; and R_1 and R_2 are the water displacement during each encoding block). The spin density function is the average propagator

scaled by the spin density. This relationship can be written generally as follows:

$$W(r, q_1, q_2) = \iint dR_1 dR_2 \Phi(r, R_1, R_2) e^{-iq_1 \cdot R_1} e^{-iq_2 \cdot R_2} \quad (1)$$

The details of numerically reconstructing Φ from the DDE signal were given previously,⁵ but briefly this is accomplished numerically using a plane wave expansion of the continuous relationship between Φ and W and spherical wave decomposition, so that the radial and angular variations of spin density function can be written separately (see equations [3] and [4] from Frank et al.⁵) in a form that allows direct numerical reconstruction of Φ at multiple radial and angular scales. From this framework, two lower dimensional quantities with direct physical interpretability were derived:

1. The radial standard deviation of Φ , which is sensitive to spatial scales by reporting the radial dependence of spin displacements averaged over all angular dependences:

$$\sigma_{R_1, R_2} \equiv \sigma(R_1, R_2) = \frac{1}{4\pi} \left(\iint d\Omega_1 d\Omega_2 [\Phi(r, R_1, R_2) - \bar{\Phi}_\Omega]^2 \right)^{1/2} \quad (2)$$

and

2. The angular standard deviation of Φ , which is sensitive to angular variations by reporting the angular dependence of spin displacements averaged over all radial dependences:

$$\sigma_{\Omega_1, \Omega_2} \equiv \sigma(\Omega_1, \Omega_2) = \frac{1}{R_{MAX}} \left(\iint dR_1 dR_2 [\Phi(r, R_1, R_2) - \bar{\Phi}_R]^2 \right)^{1/2} \quad (3)$$

where $\Omega = (\theta, \phi)$ with θ and ϕ as the polar and azimuthal angles of q , and where $\bar{\Phi}_R$ and $\bar{\Phi}_\Omega$ are the radial and angular averages of Φ , respectively.

Although both σ_{R_1, R_2} and $\sigma_{\Omega_1, \Omega_2}$ are reduced forms of the full spin displacement profile, each is a multi-dimensional tensor that characterizes diffusion properties at different radial and angular scales, respectively. These have been further simplified into scalar metrics of radial and spherical anisotropy (RA and SA, respectively) given by

$$RA = \langle \sigma_R \rangle = \int \sigma(R_1, R_2) dR_1 dR_2 \quad (4)$$

and

$$SA = \langle \sigma_\Omega \rangle = \int \sigma(\Omega_1, \Omega_2) d\Omega_1 d\Omega_2 \quad (5)$$

These two scalar metrics of anisotropy are expected to report microscopic anisotropic features of tissue that are driven by radial and angular variance in the spin displacement profile.

Two aspects of the DiTSI framework distinguish it from existing techniques for DDE signal representation, such as the cumulant expansion^{23,24} or the related correlation tensor imaging (CTI) framework.²⁵ First, signal variance from radial and angular sources is completely separable in the DiTSI framework. Second, although the limits of integration used to calculate SA and RA are over all displacement lengths and angles, respectively, it is possible to modify these to probe subsets of the spin density function, thereby sensitizing the framework metrics to specific length scale and shape ranges. In contrast, the expansion-based frameworks rely on the separation of non-Gaussian signal to report kurtosis anisotropy. These fundamental framework differences imply complementary information in the reported metrics and different dependencies on radial and angular encoding. Although expansion-based frameworks require radial encoding that supports reconstruction of kurtotic or non-Gaussian signal behavior, the DiTSI framework requires subspace sampling, in which the direction sets of the first and second PFG are identical, but the range and combination of gradient strengths are flexible.

3 | METHODS

3.1 | Brain specimens

MRI microscopy was performed for healthy brain stem and temporal lobe specimens from the same brain (no AD diagnosis during life, Braak score of IV in neuropathology report) with the objective to evaluate DiTSI metrics in anatomical structures with diverse configurations. To address the secondary objective of evaluating DiTSI metric sensitivity to pathology, a second temporal lobe specimen from a brain with AD pathology and neurodegeneration (clinical AD diagnosis during life, Braak score of VI in neuropathology report) was scanned. High-quality tissue specimens were obtained from the Banner Sun Health Brain and Body Donation Program (BBDP).²⁶ The BBDP has obtained institutional review board approval for all aspects of informed consent and protocols used in this study (please see Beach et al.²⁶ for details and additional descriptions of ethical considerations related to the BBDP procedures. Specimens from two individuals were used in this study: Subject 1 was male, age 88, with some age-related histopathology (Braak Stage IV) but no clinical diagnosis of cognitive impairment during life, and Subject 2 was a male, age 71, with clinical diagnosis of AD

in life and heavy histopathologic burden (Braak Stage VI). (For additional details, see table 1,²⁷ Subject IDs 1 and 2). The postmortem intervals for these were 17.5 h and 6.8 h, respectively, and as per BBDP protocols: Immediately following brain extraction at autopsy, specimen blocks were prepared for the temporal lobe (1-cm thickness, single hemisphere) and whole brain-stem hemisphere and immediately placed in 10% formalin for a fixation period of 48 h and then rehydrated and stored in phosphate buffered saline with preservative until MRI scanning. The temporal lobe block was trimmed to fit into a 35-mm tube, and all specimens were immersed in Fluorinert (FC-3823, 3M, St. Paul, MN) for scanning and degassed under vacuum to remove air bubbles.

Following MRI acquisition described subsequently, the specimens were sectioned and stained to visualize myelinated axons and neurites by immunohistochemistry for myelin basic protein (myelin, LSBio) and microtubule associated protein-2 (MAP2, Abcam) using established methods.²⁸ Slides were imaged using a Nikon BioPipeline Slide Scanner at 10 \times objective and resolution of 0.34 mm/pixel.

3.2 | MRI acquisition

All MRI data were collected with a Bruker 7T preclinical scanner using a 40-mm quadrature coil to transmit and receive signal. A high-resolution anatomical image was collected using a three-dimensional (3D) T₂-weighted RARE pulse sequence with 300-micron isotropic voxel size. Both SDE and DDE diffusion-weighted MRIs (DWIs) were collected using a 3D spin-echo echo-planar imaging (EPI) pulse sequence with spatial resolution of

300-micron isotropic voxel dimensions. Multishell SDE DWIs were collected using echo time (TE)/repetition time (TR) = 41/800 ms (temporal lobe) or TE/TR = 45/800 ms (brain stem), six segments, and diffusion encoding using pulse timings of $\delta = 5$ ms and $\Delta = 25$ ms with $b(\# \text{ directions}) = 1000(32)$, 2000(32), and 4000(56)s/mm² along with two unweighted images.

For DDE, a similar 3D spin-echo EPI pulse sequence was used to collect images in the same scan session as the SDE with TE/TR = 76/800 ms (temporal lobe) and TE/TR = 82/800 ms (brain stem), four segments, and cubic encoding (i.e., all 64 combinations of 8 PFG1 and 8 PFG2 directions defined by the vertices of a cube, over a range of the 9 b -value pairs $b_1/b_2 = 1000/1000$, 1000/2000, 1000/4000, 2000/1000, 2000/2000, 2000/4000, 4000/1000, 4000/2000, and 4000/4000 s/mm²). In different scans sessions, the specimens were imaged again with TE/TR = 78/400 ms, four segments, and 250-micron isotropic resolution and using more comprehensive dodecahedral angular sampling (i.e., all 400 combinations of 20 PFG1 and 20 PFG2 directions defined by the vertices of a dodecahedron) with a range of b_1/b_2 combinations (1200 DWIs) with $b_1/b_2 = 1000/1000$, 1000/2000, and 2000/2000 s/mm². These encoding schemes are shown in Figure 1. For all DDE scans and for both specimens, the first and second PFG blocks had identical timings with $\delta = 5$ ms, $\Delta = 25$ ms, and mixing time $\tau_m = 16$ ms between them.

3.3 | Radial and angular DDE subsets

Signal and metric map dependence on radial encoding was analyzed using different subsets of the fully

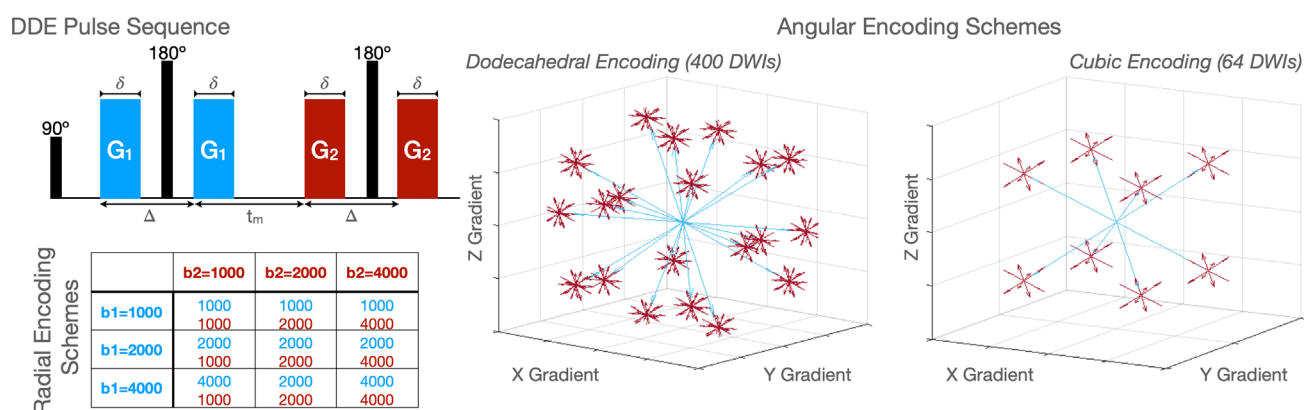


FIGURE 1 The double diffusion encoding (DDE) acquisition pulse sequence and encoding schemes used in this study. The diffusion timings (i.e., δ and Δ) were the same for both diffusion pulsed field gradient blocks, although different gradient strength combinations for first and second blocks were repeated for all angular encoding directions in the dodecahedral and cubic encoding schemes, which are shown at right. For all panels, the first and second pulsed field gradient (PFG) blocks correspond to blue and red shapes and values, respectively. DWI, diffusion-weighted image.

sampled cubic-encoded DDE data described previously. In addition to the full set (576 DWIs), $b_1/b_2 = 1000/1000$, $1000/2000$, $2000/1000$, and $2000/2000$ s/mm² (256 DWIs), $b_1 = b_2 = 1000$ s/mm² (64 DWIs), $b_1 = b_2 = 2000$ s/mm² (64 DWIs), and $b_1 = b_2 = 4000$ s/mm² (64 DWIs) were extracted as radially dependent subsets.

Dependence on angular encoding was analyzed using different subsets of the fully sampled dodecahedral encoded DWI set, which had 20×20 directions or 400 DWIs for each $b_1/b_2 = 1000/1000$, $1000/2000$, $2000/2000$ s/mm² for a total of 1200 DWIs. Subsets with full radial sampling (i.e., all with $b_1/b_2 = 1000/1000$, $1000/2000$, $2000/2000$ s/mm²) were generated by down-sampling the subspace directions from the full 20×20 to partial sampling with 15×15 , 13×13 , 10×10 , 7×7 , and 5×5 directions. In these sets, antipodal symmetry (i.e., necessary inclusion of opposite direction vectors) was not preserved. Because the 20×20 dodecahedral subspace subsumes the 8×8 cubic subspace used in the other parts of this study, an additional 8×8 subset was created with cubic sampling, and this set maintains antipodal symmetry.

3.4 | Diffusion reconstruction

3.4.1 | MRI processing

Apparent motion and distortion corrections were made for all SDE and DDE data sets using the *TORTOISE* image-processing pipeline.²⁹

Four SDE frameworks and one DDE framework were selected for comparison with DiTSI based on their established application in numerous past studies and that each framework includes an anisotropy metric that is distinct from the others. SDE frameworks investigated included DTI,⁸ neurite orientation distribution and dispersion imaging (NODDI),¹¹ diffusion kurtosis imaging (DKI),⁹ and mean apparent propagator MRI (MAP-MRI).¹⁰ Traditional computation of the diffusion tensor and mapping fractional anisotropy (FA) as well as estimation of the mean apparent propagator and mapping of the propagator anisotropy (PA) was implemented using the *TORTOISE* software.²⁹ The NODDI model was implemented and orientation dispersion index (ODI) maps generated using ex vivo model and parameters with the NODDI *MATLAB* toolbox,¹¹ and the DKI framework was used to fit the appropriate DWI data ($b = 1000$ and 2000 only) and to map the kurtosis microscale anisotropy (DKI- μ FA)^{30–32} using the DiPy libraries and implementation.³³ The additional DDE framework investigated was correlation tensor imaging (CTI),²⁵ which was implemented for the full

dodecahedral encoded set described previously using DiPy libraries, and the metric of kurtosis anisotropy (CTI- K_{aniso}) was compared with RA and SA maps from the same DDE data. All DiTSI analysis was performed using custom C/C++ software as described in Frank et al.⁵

3.4.2 | Framework comparisons

DiTSI metric maps of SA and RA were compared with FA in both the temporal lobe and brain stem specimens. Additionally, ODI, DKI- μ FA, PA, and CTI- K_{aniso} were compared with SA, RA, and FA to evaluate a broad range of frameworks and metrics. Because all cubic DDE and SDE DWIs were collected in the same scan session, there was no need for image or map registration for these. The dodecahedral-encoded DDE set was collected in a different scan session so that registration was necessary, and this was accomplished using ANTs registration software³⁴ to perform affine and diffeomorphic registration of identical structural scans collected during each scan session. The resulting transform was applied to the RA and SA maps from the dodecahedral-encoded set to bring them into the same space as the primary data sets of cubic DDE and SDE.

Voxelwise comparisons were made using composite maps akin to microscopy methods to assess colocalization of different fluorophores. For MRI composite mapping, the ImageJ³⁵ color channels were used to assign FA to the red channel and SA or RA to the green channel, so that regions of colocalized contrast were pseudo-colored yellow, whereas voxels with contrast driven by a single metric were colored red or green accordingly.

Additionally, inspection of three targeted regions was performed using a priori knowledge of cellular morphology, tissue complexity, and existing diffusion metric performance in these regions. The GM/WM interface of the cortex was included as a region known to have intermingled myelinated axon bundles and cell neurites with disperse orientations, so that μ FA is expected to be high while macroscale anisotropy is expected to be low. The hippocampal layers were inspected, as they have been well characterized by diffusion MRI³⁶ and polarized light imaging³⁷ in previous studies and known to have layers predominated by coherent neurites and layers in which axon bundles such as the perforant path (PP) intermingle with the neurite fields of the lacunosum moleculare and dentate molecular layer as they cross them. Finally, the brain stem was included, given the wide range in complexity and microstructure of the tracts, bundles, and cellular regions within this structure and previous mapping and diffusion MRI studies by other researchers.^{38,39}

3.4.3 | Radial and angular encoding

The use of two separate encoding blocks for DDE acquisition and their respective diffusion weighting strengths (e.g., as given by b -value) and direction both with respect to the scanner and object and with relative to each other were evaluated by comprehensive sampling and subset analysis of the data. Signal and metric map dependence on radial encoding was analyzed using all b_1/b_2 combinations for 1000, 2000, and 4000 s/mm², and dependence on angular sampling was analyzed by comparison of the cubic ($8 \times 8 = 64$ DWI direction sets) and dodecahedron ($20 \times 20 = 400$ DWI direction sets). These encoding schemes are shown in Figure 1.

Direct metric comparisons across frameworks or for maps from subsampled encoding were made using two-dimensional (2D) histograms with the *R* software hexbin package (*R* version 4.2.2; <https://cran.r-project.org/package=hexbin>).

Both temporal lobe tissue specimens used in the present study were also scanned separately in a different but related set of SDE experiments that has been published previously.²⁷

4 | RESULTS

High-quality maps of the human temporal lobe and brain stem were calculated from SDE DWIs for the primary anisotropy metrics of widely used SDE frameworks, specifically DTI FA, DKI- μ FA, and MAP-MRI PA, and from DDE DWIs for DiTSI SA and RA and CTI- K_{aniso} . These maps

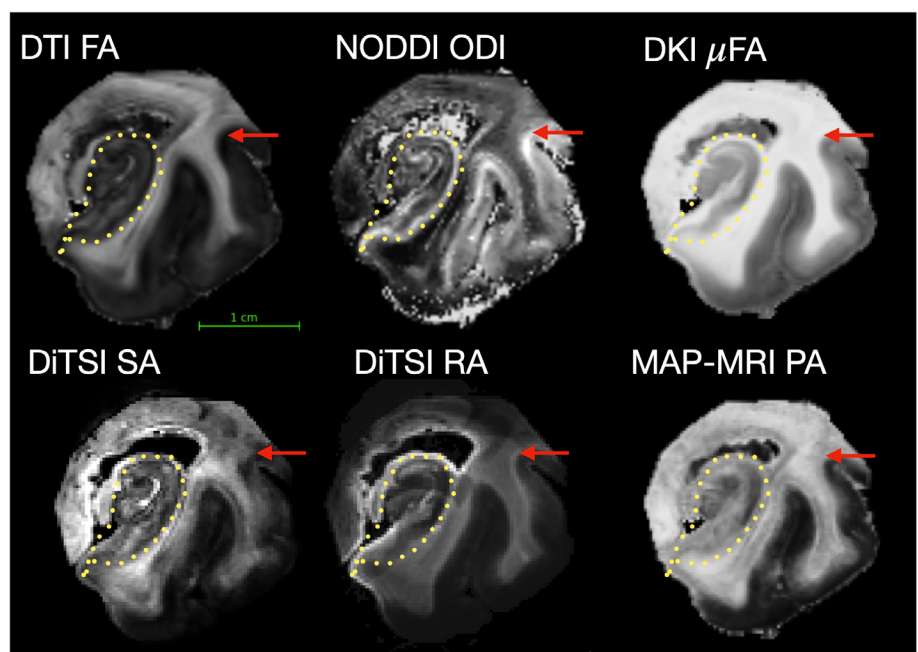
were compared across frameworks and to histologic staining for myelin and neurites, to provide a detailed description of the relationships among SA, RA, and the tissue environment as well as to identify distinct and overlapping metric information across all frameworks. In the first part of Section 4, a comparative analysis of metrics is provided in the context of tissue regions with complex microstructure known to challenge dMRI frameworks—the GM/WM interface of the cortex, hippocampus, and the brain stem. In the second part of Section 4, an evaluation of the radial and angular encoding dependencies of the DiTSI framework is presented.

4.1 | Signal representation in complex tissue environments by SA and RA

4.1.1 | The GM/WM interface of the cortex is delineated by RA

In this region, FA was observed to be low compared with the adjacent WM, and ODI was high compared with both adjacent GM and WM. The SA metric followed a similar pattern as FA, whereas the RA was found to have greater values in this region than in the adjacent cortex and also greater than the body of white matter that underlies it (Figure 2, red arrows; Figure 3, white boxes). Non-Gaussian SDE frameworks of DKI and MAP-MRI were also able to represent microscale anisotropy in this interface region as high values of DKI- μ FA and PA (Figure 2, red arrows; Figure 3, white boxes). Unlike RA, neither metric demonstrated contrast between the

FIGURE 2 Metric maps at the level of the hippocampus in a human temporal lobe specimen. diffusion tensor imaging (DTI) fractional anisotropy (FA), neurite orientation distribution and dispersion imaging (NODDI) orientation dispersion index (ODI), kurtosis microscale anisotropy (DKI- μ FA), mean apparent propagator MRI (MAP-MRI) propagator anisotropy (PA), and diffusion tensor subspace imaging (DiTSI) spherical and radial anisotropy (SA and RA) maps are shown with dotted yellow line to indicate the hippocampus, and red arrow to indicate the gray-matter/white-matter interface.



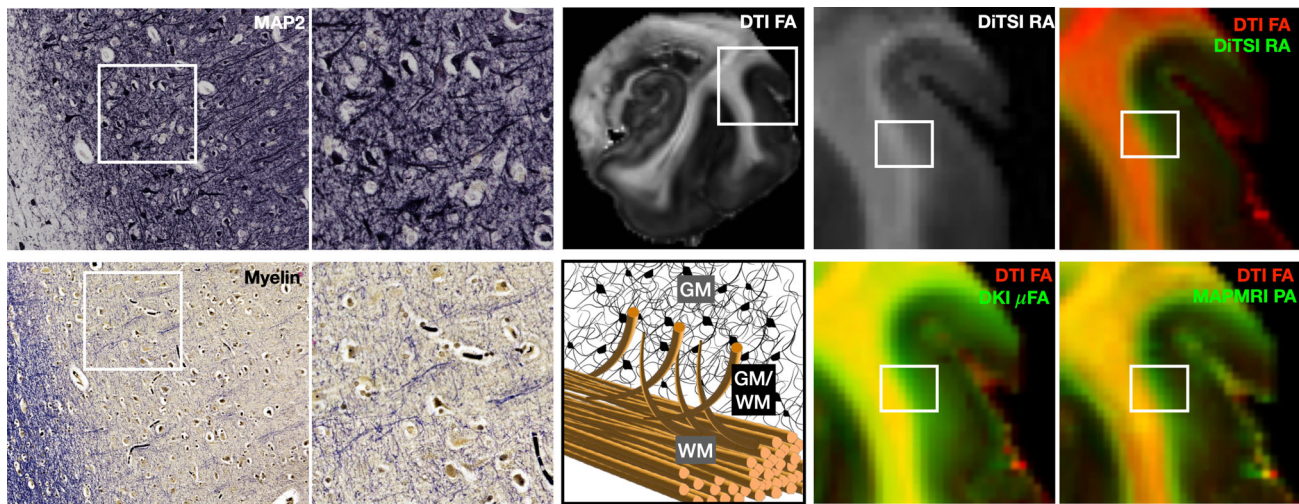


FIGURE 3 Gray-matter/white-matter interface (GM/WM) comparison of radial anisotropy (RA), kurtosis microscale anisotropy (DKI- μ FA), and mean apparent propagator MRI (MAP-MRI) propagator anisotropy (PA) with fractional anisotropy (FA). Histologic staining of myelin and neurites (MAP2) in the same tissue and region confirm the high microscale anisotropy but geometric complexity of this region, which is depicted as a labeled illustration. Magnified metric and composite maps (FA, red; RA, DKI- μ FA, and PA, green) show high RA, DKI- μ FA, and MAP-MRI PA values in the GM/WM region of low FA. FA, DKI- μ FA, and PA values are high in the body of the WM, whereas RA values are lower. White boxes indicate magnified regions.

interface regions and the body of the WM. Composite maps (Figure 3) were used to confirm contrast differences at the GM/WM interface between FA and each metric, and the microstructural tissue environment was validated using myelin histology in the same tissue. Based on the histology and known neuroanatomy, an illustration was prepared to describe the microstructure. Briefly, myelinated fibers of the cerebral cortex project to and from cells in the middle layers of the cortex in such a way that they must traverse deep layer neurites that are generally not oriented in the same direction. As such, this interface between GM and WM is predominated by strong microstructural anisotropy of the fibers and local neurites but highly disperse architecture across these intermingled crossing fibers and projections (see illustration and histologic validation in Figure 3).

4.1.2 | Unmasking of the hippocampus perforant pathway by DiTSI-RA, DKI- μ FA, and PA metrics

Although the hippocampus is considered to be a GM structure, its neurons are organized in such a way that dense, coherent neurites and crossing projection fibers of the trisynaptic pathway give rise to anisotropy differences across the layers that are detectable by diffusion MRI.³⁶ The most evident finding across the framework anisotropy metrics was the visibility of the perforant path (PP; white arrowheads Figure 4) within the lacunosum-molecular by the RA, DKI- μ FA, and PA metrics, whereas FA and SA

were relatively low. Notably, the spatial pattern of contrast was different across RA, DKI- μ FA and PA, perhaps due to non-Gaussian signal from myelin and heterogeneity of length scales.

4.1.3 | Tissue-metric relationships in the hippocampus vary across frameworks suggesting specificity

In addition to the PP, other regions and layers of the hippocampus demonstrated an unexpected degree variability in metric contrast across frameworks (Figure 2, yellow dotted line). Both FA and SA were greatest in the dentate gyrus molecular layer (dML, yellow arrowhead; Figure 4), whereas RA, DKI- μ FA, and PA were low in this region compared with surrounding tissue. This region contains dense, coherently oriented dendrites of the dentate granule cells⁴⁰ but does not contain myelinated axons, so that the SDE signal in this region is more Gaussian than in the PP, but the macroscale geometry is highly coherent, which may explain the relative contrasts of the metrics.

A further distinction of metrics was observed in the stratum radiatum layer, which is also dominated by coherent neurites but more microstructurally complex than the dML. In this region, SA, FA, and PA were relatively high compared with DKI- μ FA and RA. Together, these findings suggest that SA and RA provide distinct information with SA most sensitive to coherency, and RA most sensitive to size distributions with little dependence on the signal

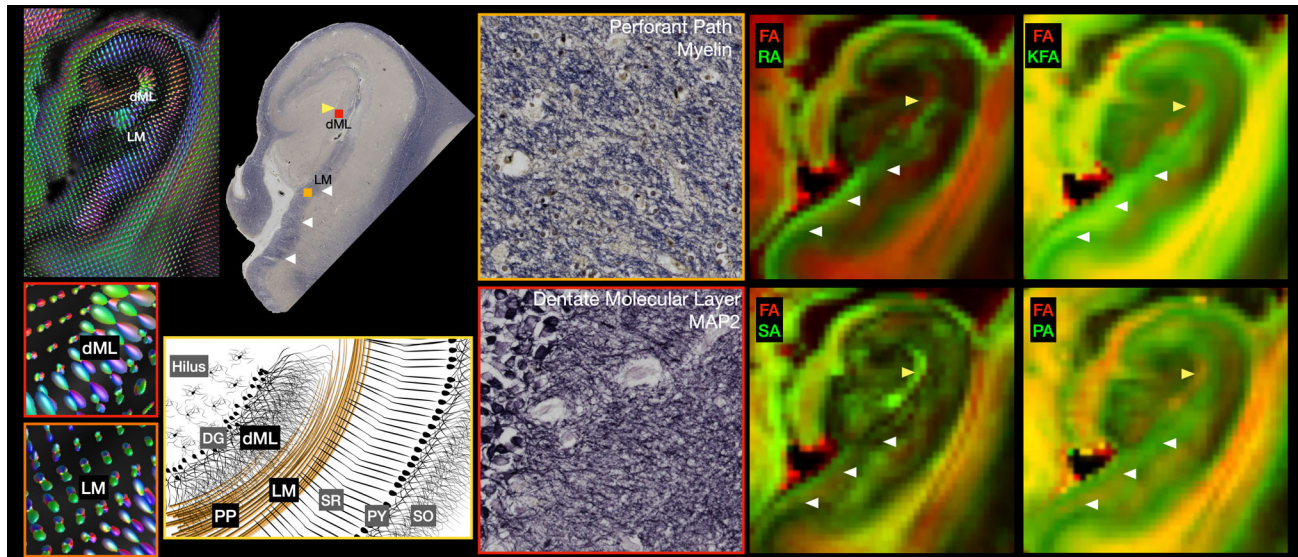


FIGURE 4 Microstructural anisotropy within hippocampal layers and regions is distinguished by radial anisotropy (RA) and spherical anisotropy (SA). Layers of the hippocampus—especially the perforant path (PP; *white arrowheads*) and the dentate gyrus molecular layer (dML; *yellow arrowhead*)—are readily identified by their orientational features on the fiber orientation distribution (FOD) maps (*left*) and the microstructural environment of PP projection fibers crossing neurites, and dML coherent dendrites was confirmed histologically. The composite maps (*right*) show regions of similarity (*yellow*) and distinction (*red*) with the fractional anisotropy (FA) metric map including unmasking of the PP by RA, kurtosis microscale anisotropy, and propagator anisotropy (PA). Colored boxes on the histology inset indicate magnified regions for microscopy, and FOD maps and other regions of the hippocampus are labeled in the illustration as dentate granule layer (DG), lacunosum moleculare (LM), stratum radiatum (SR), pyramidal cell layer (PY), and stratum oriens (SO).

Gaussianity that appeared to more strongly influence DKI and MAP-MRI metrics.

4.1.4 | Neurodegenerative pathology prominently affects SA and RA

In addition to the healthy temporal lobe specimen reported in Sections 1.1–1.3, a specimen with AD pathology was also examined. Image acquisition, processing, and metric mapping were performed simultaneously for both specimens, as they were contained in the same tube during MRI scanning, and the maps for FA, SA, RA, DKI- μ A, and PA are shown for a longitudinal slice with both specimens at the level of hippocampus (Figure 5). Histograms for values in all tissue, hippocampus, and WM are shown for both specimens to compare quantitative differences in metric values in healthy and AD tissue. Both SA and RA showed the most prominent differences between the two specimens, and both metrics revealed a reduction in values for the AD specimen in the hippocampus and WM. RA revealed a loss of the GM/WM bright rim and appearance of punctate bright values in the WM. SA values were greatly reduced in the WM. Although FA maps appear to be the least different between AD and healthy specimens, there were observable differences in the PA and DKI μ FA maps, especially for PA in the hippocampus and cortex,

as previously reported in a related larger study.²⁷ The WM was not appreciably different for SDE metrics, but RA and SA histogram distributions were prominently decreased.

4.1.5 | Unmasking of cranial nerve fascicles in the brain stem by the SA metric

In the brain-stem specimen, near the level of the pontomedullary junction, small fiber tracts were observed by the SA map that were entirely absent from the FA, DKI- μ FA, PA, and CTI- K_{aniso} maps (yellow box, Figure 6; see S1 for CTI- K_{aniso}). These fibers correspond to the seventh cranial nerve system (CNVII), which is known to fasciculate as it travels from the CNVII nucleus to the nerve root.⁴¹ The fascicles themselves are small, myelinated, and compact. Although one of the larger fascicles appears on the FA, PA, and CTI- K_{aniso} maps (green arrowhead, Figure 6), the remaining two (magenta arrowheads, Figure 6) are not discernable from surrounding voxels in the other maps.

4.1.6 | Selectivity of SA for a subset of brain stem pathways

Although the CNVII fascicles provide evidence of unmasking new anatomic regions, most of the differences between

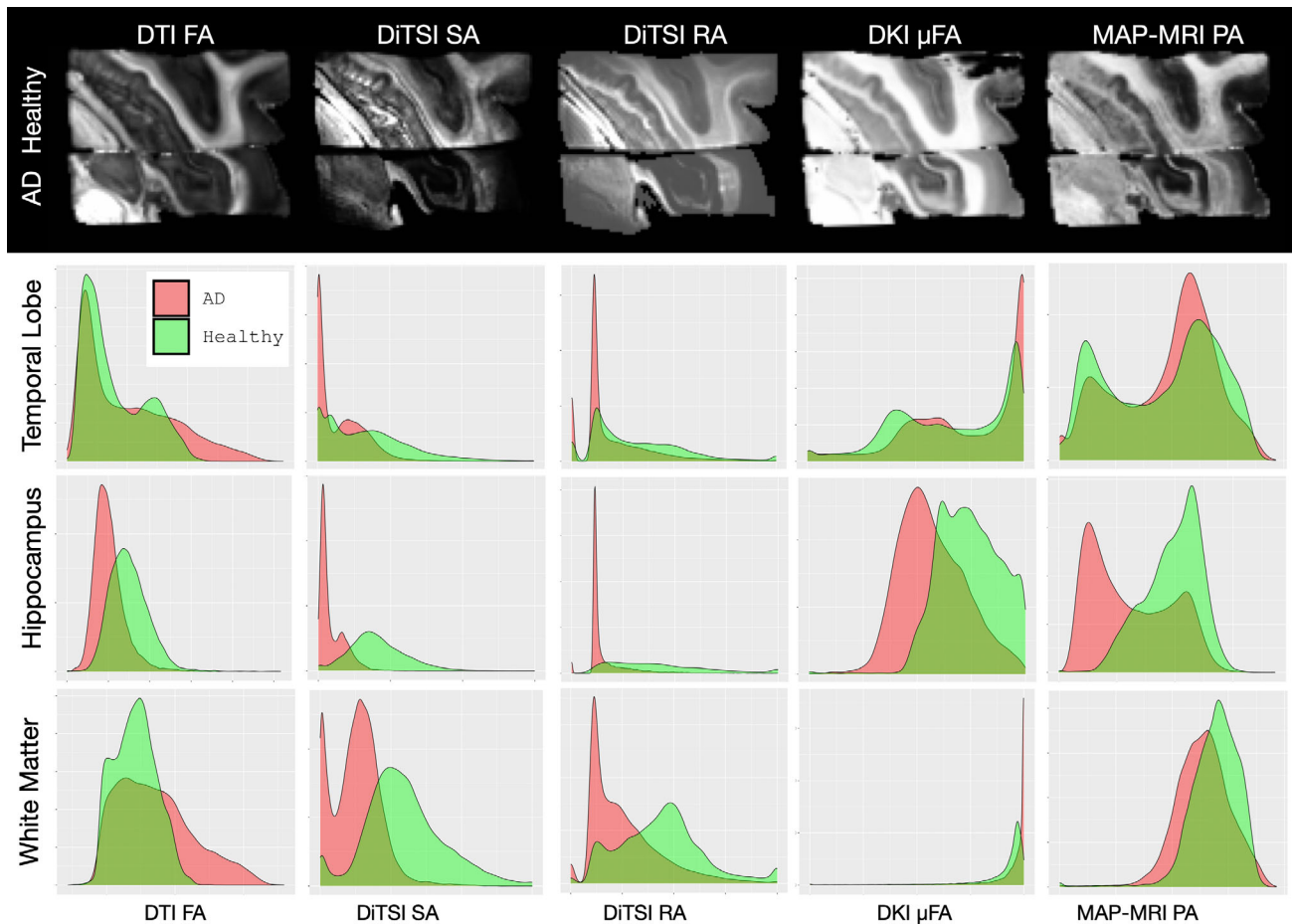


FIGURE 5 Reduction of spherical anisotropy (SA) and radial anisotropy (RA) in tissue with Alzheimer's disease (AD) pathology is more prominent than for single diffusion encoding metrics. Healthy and AD tissue specimens were imaged in the same container and processed simultaneously, as shown by the longitudinal slice view in native space for framework metrics maps. Compared with fractional anisotropy (FA), propagator anisotropy (PA) demonstrated reduced values in the AD specimen hippocampus as previously reported but not white matter, whereas SA and RA were prominently reduced in both tissue regions. DiTSI, diffusion tensor subspace imaging; DKI, diffusion kurtosis imaging; DTI, diffusion tensor imaging; MAP-MRI, mean apparent propagator MRI.

SA and other metrics by voxelwise composite map comparison were that SA calculated with the acquisition and processing parameters used was selective for a subset of regions identified by the FA map in the brain stem (Figure 7, red and green respectively). Notably, multiple fiber pathways were evident on both FA and SA (corticospinal tract [cst], medial lemniscus [ml], among others). However, several pathways (medial longitudinal fasciculus [mlf], some pontine fiber projections [pf], olivary white matter [owm], superior cerebellar peduncle [scp], among others) were absent in the SA and RA maps. GM regions were evident on the SA maps, including periventricular GM along the full extent of the brain stem and olivary nucleus. None of the non-Gaussian SDE maps or the CTI- K_{aniso} maps (Figure S2) showed strong contrast in these GM regions, although there were considerable differences between these maps and the more conventional DTI-FA map, as expected based on framework differences.

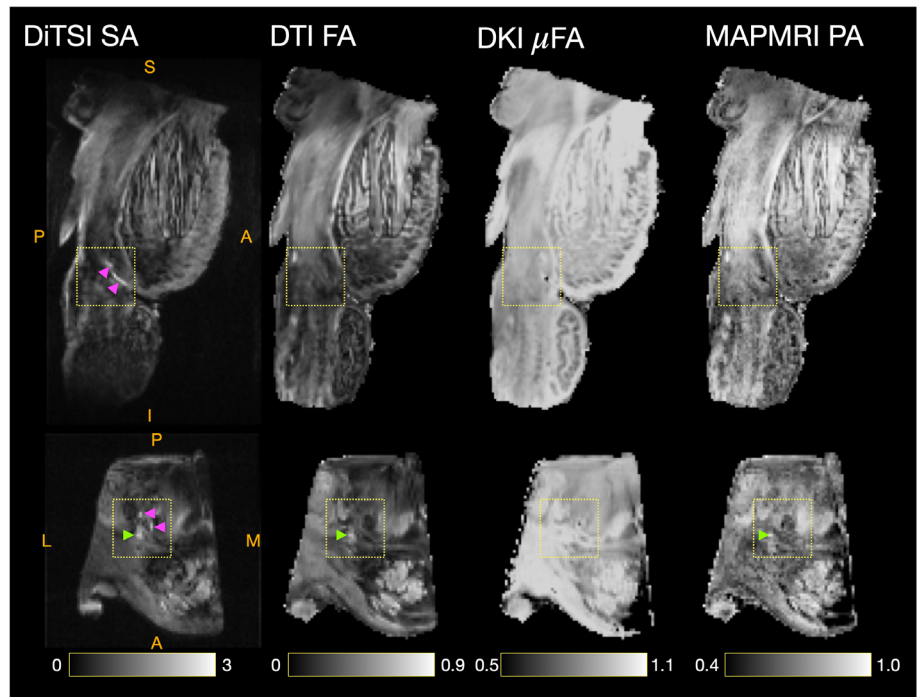
Specifically, DKI- μA and PA maps included many more voxels with high values than FA, and the CTI- K_{aniso} values were close to zero for most voxels aside from a subset of voxels with high SA values.

4.2 | DDE encoding

4.2.1 | Radial encoding influences sensitivity to size distribution

DiTSI maps generated using DDE DWIs with cubic angular sampling and five different radial sampling schemes of full (all nine b_1/b_2 combinations, $b_{\text{max}} = 4000 \text{ s/mm}^2$ 576 DWIs), reduced (four b_1/b_2 combinations, $b_{\text{max}} = 2000 \text{ s/mm}^2$, 256 DWIs), and single $b_1 = b_2$ sets (three different b-values, 64 DWIs each) are shown in Figure 8. Differential sensitivity of SA to radial encoding

FIGURE 6 Detection of the seventh cranial nerve system (CNVII) fascicles by spherical anisotropy (SA). One fascicle of the CNVII nerve is evident on fractional anisotropy (FA), propagator anisotropy (PA), kurtosis microscale anisotropy (DKI- μ A), and spherical anisotropy (SA) maps (*green arrow*), whereas two additional fascicles are evident only with SA and are absent on all other maps (*magenta arrows*). Top row shows sagittal view, and bottom row shows axial view where A = anterior, P = posterior, S = superior, I = inferior, M = medial, and L = lateral. DTI, diffusion tensor imaging.



within GM and WM were evident as the greatest range of contrast for the full and reduced set and stronger GM and WM contrast for low and high b -values, respectively. This was evidenced also in histogram plots in which the fully sampled set resulted in a broad and bimodal distribution for temporal lobe SA, whereas reduced sampling schemes resulted in SA values with decreased range and single mean distribution.

4.2.2 | Angular encoding influences SA preferentially and can be reduced

DiTSI maps generated using different subspace encoding as described in Section 3 with constant radial encoding of $b_1/b_2 = 1000/1000, 1000/2000$, and $2000/2000$ s/mm² are compared in Figures 9 and 10 at different levels of the brain stem and using 2D histogram mapping of SA and RA values from these maps. Compared with full dodecahedral encoding, decreased angular encoding resulted in region-specific loss of contrast, such as some CST pathways (see red arrow, Figure 9), but most of the metric contrast was maintained over considerable reductions. For SA, the contrast of the maps was considerably reduced for the 7×7 and 5×5 subspaces, but those with more DWIs were relatively uncompromised. RA maps showed less dependence on angular encoding, as most images were similar and 2D histograms strongly correlated across all subsampled sets.

Notably, when subsampling was accomplished by selecting only the cubic encoding directions from the

dodecahedral set, both SA and RA values were strongly affected (right columns, Figures 9 and 10) with a loss of tissue contrast similarity in the SA maps.

5 | DISCUSSION

The DiTSI framework parameterized DDE-MRI data as SA and RA metrics, to provide tissue contrast that was fundamentally distinct from metrics of other SDE and DDE frameworks. Both metrics captured microscale features within complex tissue environments, including delineation of small fascicles by SA and unmasking of microscale anisotropy by RA in tissue with mixed neurite and fiber composition. The mapping and comparative analysis of SA and RA for postmortem human specimens aligns with the long-established observations that DDE is sensitized to the geometry of small features instead of the arrangement of structures within the voxel^{13,14,16,18,20} and capable of reporting microstructural features that are not possible using SDE signal representation. Within DDE frameworks, the two main advancements of DiTSI are (i) moving beyond fiber-dependent encoding in which the PFG directions are chosen based on a priori knowledge of the fiber geometry to a subspace-based encoding and (ii) independence from an analytic framework based on Gaussian and non-Gaussian water displacement.

The DiTSI metric of RA, in which the spin density function is integrated over all angles sampled to report radial dependencies, demonstrated increased specificity for multifiber tissue environments. This is evidenced as

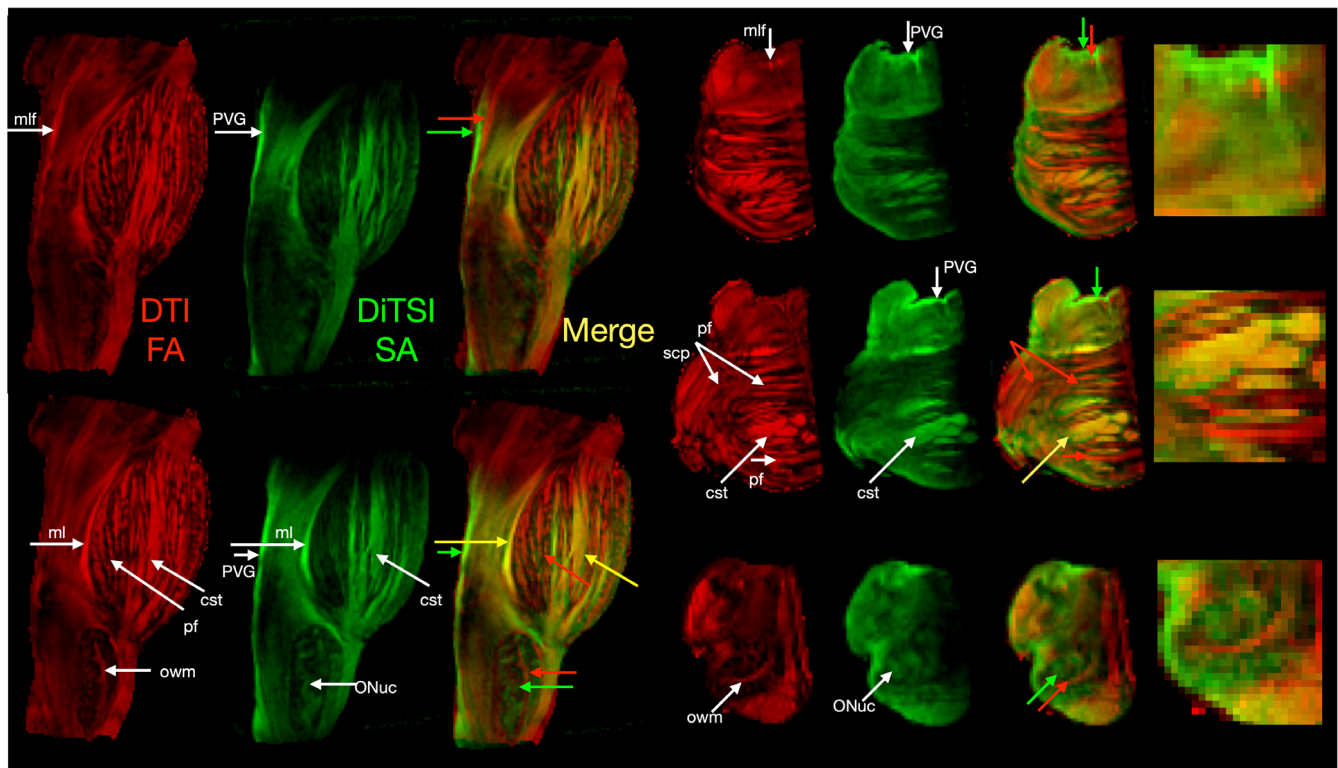


FIGURE 7 Composite maps for voxelwise comparison of fractional anisotropy (FA; red) and spherical anisotropy (SA; green) in the brain stem. Regions of overlap (yellow arrows) include the corticospinal tract (cst) and medial lemniscus (ml), and regions of FA detectable fibers without SA contrast (green arrows) include the medial longitudinal fasciculus (mlf), pontine fibers (pf), and superior cerebellar peduncles (scp). Gray-matter regions with strong SA contrast in the absence of FA contrast (red arrows) include the periventricular gray matter (PVG) and the olivary nucleus (ONuc). DiTSI, diffusion tensor subspace imaging; DTI, diffusion tensor imaging.

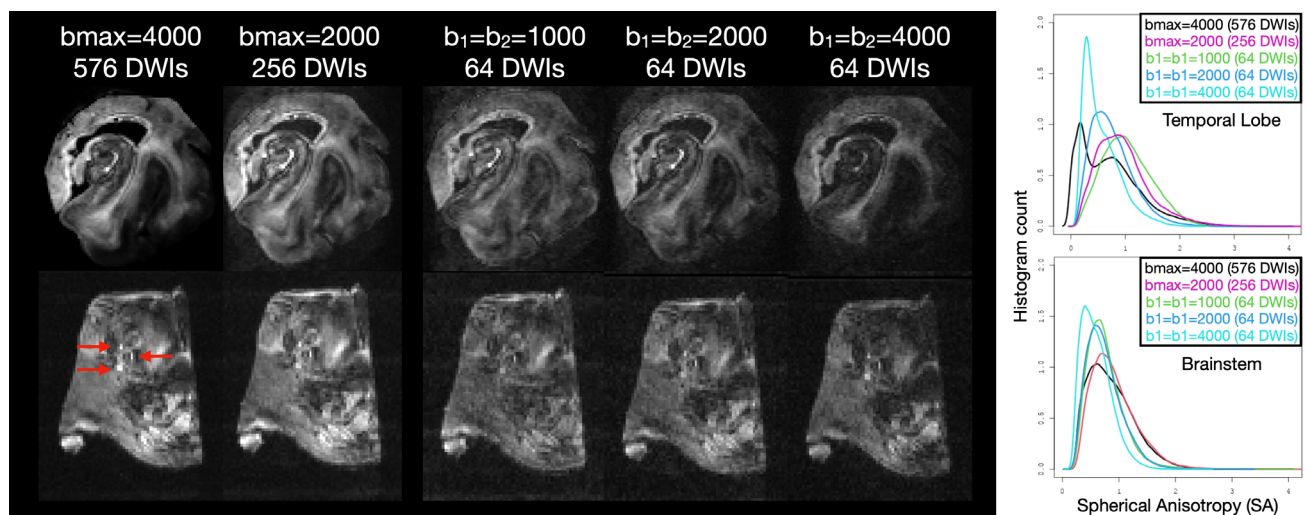


FIGURE 8 Radial encoding influences the distribution of spherical anisotropy (SA) values in temporal lobe (top) and brain stem (bottom) specimens. Contrast within gray-matter regions was greater for lower b -value data, whereas small fascicles (red arrows) were most pronounced for stronger diffusion weighting. Differences in the shape and median of histogram distributions of SA were evident for different encoding schemes. DWI, diffusion-weighted image.

high contrast in regions known to have small bundles of myelinated axons projecting through complex fields of neurites, appearing as a rim in the GM/WM boundary

and resembling the myelin histology images for of the PP in the hippocampus. The combined predominance of two different sized anisotropic structures—the myelinated

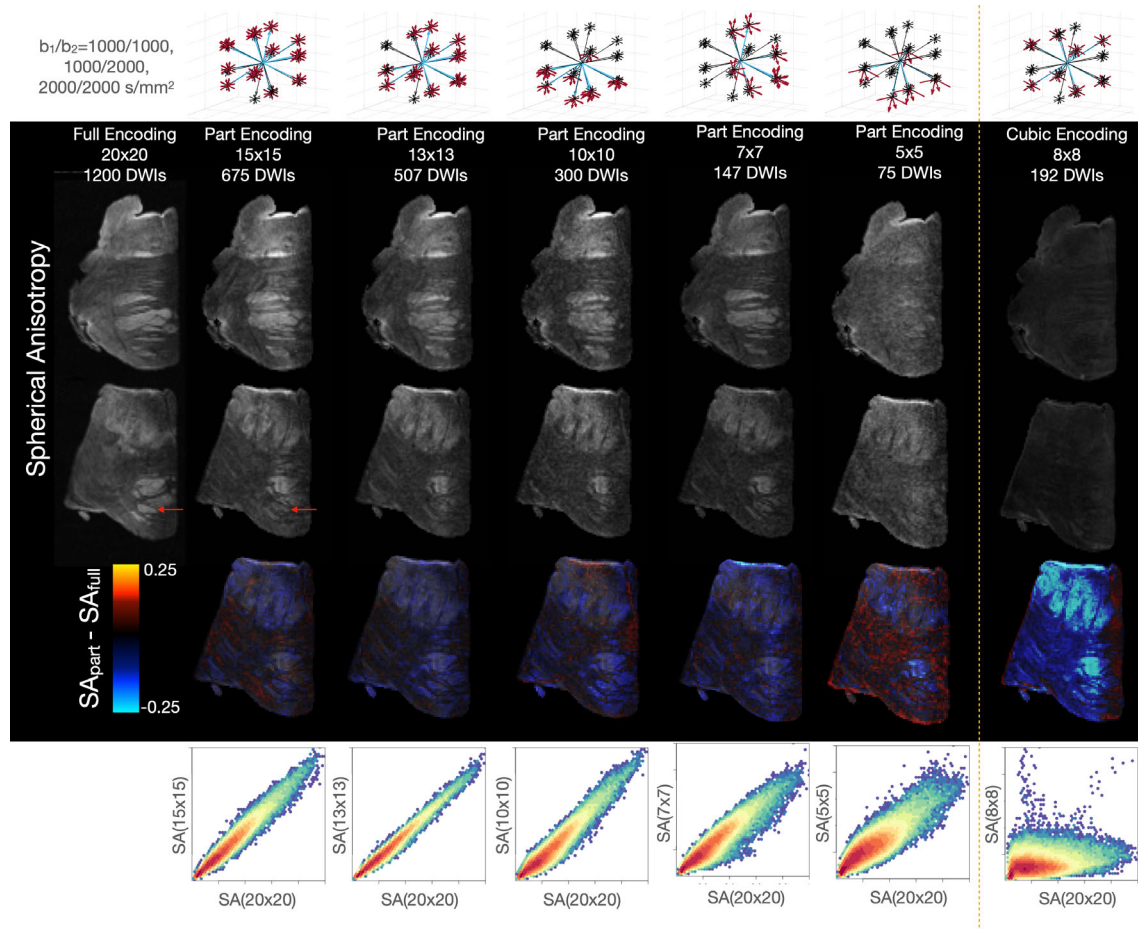


FIGURE 9 The influence of angular encoding on spherical anisotropy (SA) was evaluated using subsampled data sets according to the vector plots and labels at top as described in the text. Subtle changes in neuroanatomical mapping were observed for reduced angular encoding (*red arrow*), but for many voxels, little qualitative change or difference map change was observed. For the lowest angular sampling (5×5 subspaces) SA maps, difference maps and two-dimensional histograms showed prominent changes. Undersampling to cubic encoding (*right column*) resulted in loss of contrast similarity and prominent differences from the fully sampled maps.

axons and the neurites—may drive high RA independent of their incoherent orientation. This interpretation is supported by the contrast between these regions and adjacent coherent WM for which RA was low. Notably, the DKI- μ FA and MAP-MRI PA metrics were also high in the PP and GM/WM interface but with lack of contrast to the adjacent body of WM. This may suggest a different mechanism for sensitivity to microscale anisotropy based on non-Gaussian signal, potentially from restricted myelin water.

Mapping of the SA metric—in which the spin density function is integrated over all radial dependencies to measure angular dependence—revealed new fibers not observed by any other SDE or DDE metric such as the CNVII fascicles, which suggests high specificity for some aspect of the microstructure of these tracts compared with their complex surroundings. The observation that CNVII SA contrast was greatest for stronger DDE weighting supports the interpretation that the smaller dimensions of the

CNVII fibers are driving the selectivity to visualize this structure. The CTI anisotropy metric, K_{aniso} , did not reveal these small fascicles despite using the same DDE data for reconstruction, but K_{aniso} was distinct and more selective (i.e., less positive voxels) than any other metric. Potentially, this can be explained by separability of signal relationships based on Gaussianity and kurtosis in the CTI framework. A second explanation could be poor suitability of subspace DDE encoding to support CTI signal representation.

In other regions, SA maps were in many ways qualitatively similar to FA maps, especially for coherent WM. A likely interpretation is that SA is driven by coherency of same-sized structures. For example, both FA and SA provided strong contrast showing the dML of the hippocampus, a uniform and highly coherent dendrite field without myelinated fibers. However, direct composite map comparisons in the brain stem showed common contrast in only a subset of the tracts observed by FA. For example, the ml but not the mlf were evident by SA, even though

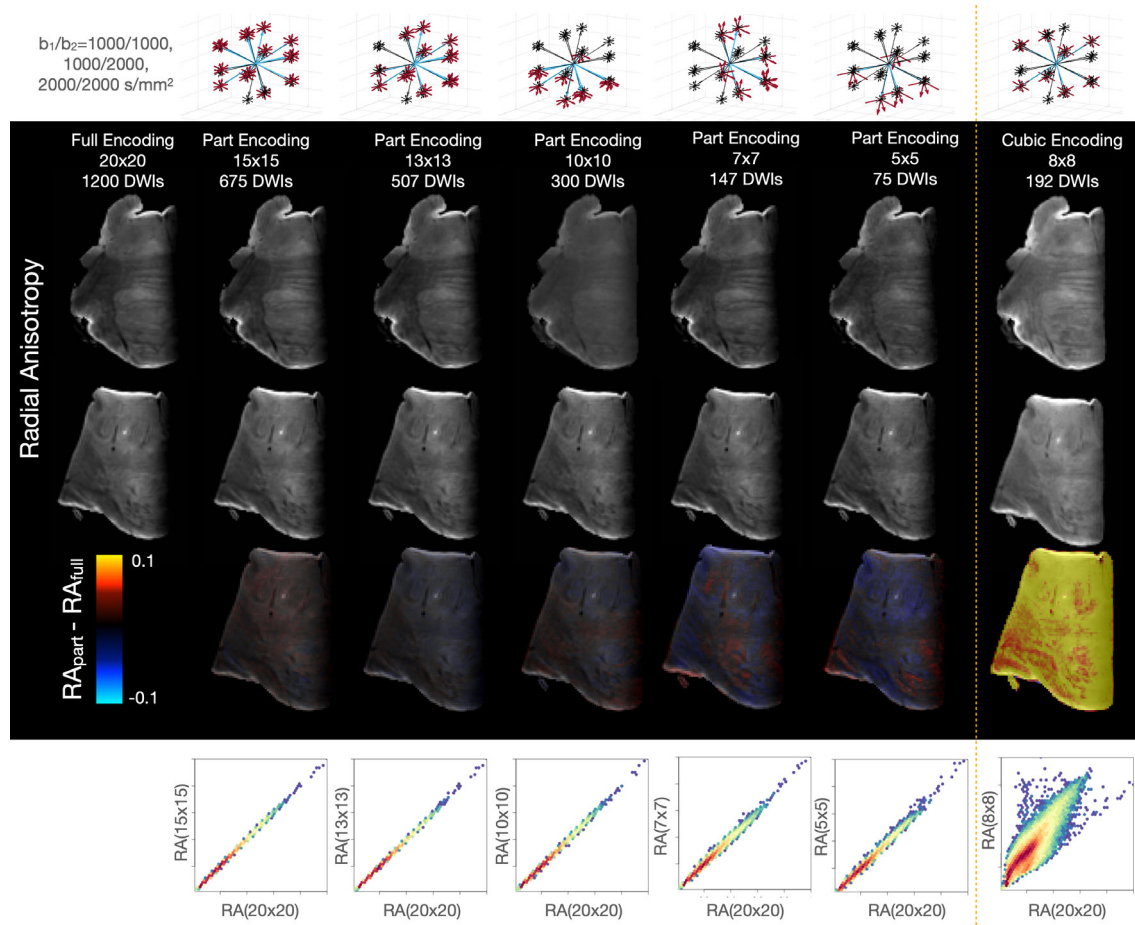


FIGURE 10 The influence of angular encoding on radial anisotropy (RA) was evaluated using subsampled data sets according to the vector plots and labels at top as described in the text. Little qualitative changes were observed in contrast across all subsampled sets, even the lowest (5×5), although difference map and two-dimensional histogram changes were evident for one 10×10 subspace and for the 7×7 subspace. Undersampling to cubic encoding (right column) resulted in prominent increases in RA values, although similar tissue contrast was maintained. DWI, diffusion-weighted image.

both are heavily myelinated tracts of similar microstructure and dimensions. There are numerous possible interpretations for these discrepancies that will be studied in the future, including mixed fiber content of pathways (e.g., myelinated and unmyelinated), different degree of axonal branching, or varicosity and tract-specific presence of inflammatory cells.

Both SA and RA metrics were highly sensitive to pathologic changes in the AD temporal lobe specimen as compared with the healthy control specimen. Previous study of more specimens using SDE-only frameworks²⁷ strongly suggests that loss of cellular microstructure is the primary underlying pathologic change. In the previous work, diffusivity was increased and kurtosis and PA were decreased for late-stage hippocampal tissue at the highest Braak stage (VI), which is in part defined by degeneration of the cells and their processes.⁴² Although the present results also demonstrate reduced PA in the hippocampus for the specimens studied, the additional finding that

SA and RA are reduced for both hippocampal and WM regions, and the more prominent decrease in these metrics than for PA, suggest greater sensitivity to degenerative processes.

The influence of encoding parameters on DiTSI metrics—or any DDE signal representation framework for that matter—is of central importance, given the many more degrees of freedom in the DDE acquisition paradigm than for SDE. In this study, timings of the PFG encodings (δ , Δ , and τ_m) were not explored, although it will be important for future studies to address these in a systematic manner, such as using Monte Carlo simulations.^{43,44} In the present study, radial and angular encoding parameters (b -values b_1 , b_2 , and b -vector directions) were systematically evaluated by collection of large data sets and subsampling. The radial encoding or range of b -values that must be collected to support meaningful signal reconstruction is perhaps the most critical parameter for SDE and DDE experiments alike. Although it is possible for

DiTSI to reconstruct the signal from a single b -value (e.g., $b_1 = b_2 = 1000 \text{ s/mm}^2$), the optimal encoding should span a range of b -values but also include different b -value pairs. Importantly, the lack of analytical form for the DiTSI framework does not require limits on the minimum, maximum, or preferred b -values for validity of the reconstruction, as is the case for diffusion and kurtosis-based frameworks. This consideration is the most likely explanation of many of the differences in metric maps observed in the present study. Of course, an optimal range for diffusion weighting is still inherent for DiTSI via signal-tissue relationships in that the most complete DDE signal representation will be supported by data collected over the range that most fully probes the signal dependence on length scales and shapes present in the tissue. In this study, DDE data with the greatest range of weighting (between 1000 and 4000 s/mm^2) and with b_1/b_2 combinations of mixed strengths provided maps with the greatest range of contrast across tissue types. Enough so that the histogram behavior for the most comprehensive sampling scheme was bimodal and spanned all metric values from subsampled DDE sets. This is in contrast to the known dependences of DTI metrics on SDE sampling ranges, which can be either biased or skewed depending on the range of b -values used.⁴⁵

Angular encoding in the DDE paradigm is a source of sensitivity to microstructural dimensions, and often the imaging experiment must be parameterized so that the first encoding block aligns parallel or perpendicular with a known fiber orientation, and the signal behavior with respect to the angle between the first and second encoding vectors can be used to capture diameter information.^{18,46,47} The DiTSI framework instead relies on subspace encoding in which the 3D representation of the spin density function is reconstructed from data collected with matched first and second PFG vectors over a range of radial encoding. In this study, we collected a large subspace using a 20-direction vector set so that for each of three b_1/b_2 pairs, $20 \times 20 = 400$ DWIs were collected for a total of 1200 DDE-weighted volumes. This encoding is unlikely to ever have clinical use, but in this study provided a set of “fully sampled” angular encoding for comparison of maps generated with subsampled DWI sets. In the subsampling analysis, neither RA nor SA metrics were strongly affected by decreasing the angular sampling except in the case of very low angular resolution (i.e., 5×5) for SA and for cubic sampling for both SA and RA. The stronger dependence of SA maps on angular sampling is intuitive, given the angular dependence of the metric. The cubic sampling scheme consists of four sets of antipodal weighting directions, whereas other types of subsampling did not maintain antipodal pairs, which implies that reduced angular sampling schemes should

favor greater sampling of unique angles over maintenance of antipodal symmetry.

In conclusion, the DiTSI framework captures information about microscale shape and size that is fundamentally accessible by DDE and not SDE frameworks and so can provide maps that are more selective. Accordingly, the SA and RA summary metrics provide contrast that is unique from SDE anisotropy metrics of FA, PA and DKI- μ A, and driven by microscale features of the underlying tissue environment as demonstrated here in postmortem specimens. However, these findings must be expanded to a quantitative analysis across many specimens and migrated to in vivo imaging. Future directions also include 3D Monte Carlo simulations to more comprehensively understand metric dependence on the many pulse-sequence parameters of the DDE acquisition and the dependence on tissue composition and architecture. Finally, the high dimensionality of the DiTSI spin displacement function expansion opens multiple avenues to develop more specific microstructural MRI markers by constraining the radial and angular ranges for signal reconstruction.

AFFILIATIONS

¹Department of Biomedical Engineering, University of Arizona, Tucson, Arizona, USA

²Department of Medical Imaging, University of Arizona, Tucson, Arizona, USA

³Banner Sun Health Research Institute, Sun City, Arizona, USA

⁴Department of Psychiatry, School of Medicine, University of California San Diego, California, USA

⁵Center for Scientific Computation in Imaging, University of California at San Diego, La Jolla, California, USA

⁶Institute of Engineering in Medicine, University of California at San Diego, La Jolla, California, USA

⁷Center for Functional MRI, University of California at San Diego, La Jolla, California, USA

⁸Department of Radiology, University of California at San Diego, La Jolla, California, USA

ACKNOWLEDGMENTS

This research was supported by National Institute on Aging (NIA)/National Institutes of Health (NIH) grants R03AG071903 and R01AG079280. All MR imaging was performed in the University of Arizona's (UA) translational bioimaging resource and made possible by National Institutes of Health grant (S10 OD025016). The authors thank the comparative pathology core lab for their assistance with tissue sectioning, and the UA tissue acquisition and cellular/molecular analysis for microscopy services. All image processing was performed using the UA High Performance Computing resources. The Brain and Body Donation Program has

been supported by the National Institute of Neurological Disorders and Stroke (U24 NS072026 National Brain and Tissue Resource for Parkinson's Disease and Related Disorders), the NIA (P30 AG19610 and P30AG072980, Arizona Alzheimer's Disease Center), the Arizona Department of Health Services (contract 211002, Arizona Alzheimer's Research Center), the Arizona Biomedical Research Commission (contracts 4001, 0011, 05-901, and 1001 to the Arizona Parkinson's Disease Consortium), and the Michael J. Fox Foundation for Parkinson's Research.

ORCID

Elizabeth B. Hutchinson  <https://orcid.org/0000-0002-3374-5469>

REFERENCES

- Alexander AL, Lee J, Lazar M, Field AS. Diffusion tensor imaging of the brain. *Neurotherapeutics*. 2007;4:316-329. doi:10.1016/j.nurt.2007.05.011
- Alexander DC, Dyrby TB, Nilsson M, Zhang H. Imaging brain microstructure with diffusion MRI: practicality and applications. *NMR Biomed*. 2019;32:e3841. doi:10.1002/nbm.3841
- Andica C, Kamagata K, Hatano T, et al. MR biomarkers of degenerative brain disorders derived from diffusion imaging. *J Magn Reson Imaging*. 2020;52:1620-1636. doi:10.1002/jmri.27019
- Reddy CP, Rathi Y. Joint multi-fiber NODDI parameter estimation and tractography using the unscented information filter. *Front Neurosci*. 2016;10:166. doi:10.3389/fnins.2016.00166
- Frank LR, Zahneisen B, Galinsky VL. JEDI: joint estimation diffusion imaging of macroscopic and microscopic tissue properties. *Magn Reson Med*. 2020;84:966-990. doi:10.1002/mrm.28141
- Magdoo KN, Avram AV, Sarlls JE, Dario G, Basser PJ. A novel framework for in-vivo diffusion tensor distribution MRI of the human brain. *Neuroimage*. 2023;271:120003. doi:10.1016/j.neuroimage.2023.120003
- Stejskal EO, Tanner JE. Spin diffusion measurements: spin echoes in the presence of a time-dependent field gradient. *J Chem Phys*. 1965;42:288-292. doi:10.1063/1.1695690
- Basser PJ, Mattiello J, LeBihan D. MR diffusion tensor spectroscopy and imaging. *Biophys J*. 1994;66:259-267. doi:10.1016/S0006-3495(94)80775-1
- Jensen JH, Helpert JA, Ramani A, Lu H, Kaczynski K. Diffusional kurtosis imaging: the quantification of non-Gaussian water diffusion by means of magnetic resonance imaging. *Magn Reson Med*. 2005;53:1432-1440. doi:10.1002/mrm.20508
- Özarslan E, Koay CG, Shepherd TM, et al. Mean apparent propagator (MAP) MRI: a novel diffusion imaging method for mapping tissue microstructure. *Neuroimage*. 2013;78:16-32. doi:10.1016/j.neuroimage.2013.04.016
- Zhang H, Schneider T, Wheeler-Kingshott CA, Alexander DC. NODDI: practical in vivo neurite orientation dispersion and density imaging of the human brain. *Neuroimage*. 2012;61:1000-1016. doi:10.1016/j.neuroimage.2012.03.072
- Tournier J, Calamante F, Connelly A. MRtrix: diffusion tractography in crossing fiber regions. *Int J Imaging Syst Technol*. 2012;22:53-66. doi:10.1002/ima.22005
- Cory DG, Garroway AN, Miller JB. Applications of spin transport as a probe of local geometry. *Abstr Pap Am Chem S*. 1990;199:105.
- Mitra PP. Multiple wave-vector extensions of the NMR pulsed-field-gradient spin-echo diffusion measurement. *Phys Rev B*. 1995;51:15074-15078.
- Cheng Y, Cory DG. Multiple scattering by NMR. *J Am Chem Soc*. 1999;121:7935-7936. doi:10.1021/ja9843324
- Callaghan PT, Komlos ME. Locally anisotropic motion in a macroscopically isotropic system: displacement correlations measured using double pulsed gradient spin-echo NMR. *Magn Reson Chem*. 2002;40:S15-S19. doi:10.1002/mrc.1122
- Koch MA, Finsterbusch J. Compartment size estimation with double wave vector diffusion-weighted imaging. *Magn Reson Med*. 2008;60:90-101. doi:10.1002/mrm.21514
- Benjamini D, Komlos ME, Holtzclaw LA, Nevo U, Basser PJ. White matter microstructure from nonparametric axon diameter distribution mapping. *Neuroimage*. 2016;135:333-344. doi:10.1016/j.neuroimage.2016.04.052
- Yang G, Tian Q, Leuze C, Wintermark M, McNab JA. Double diffusion encoding MRI for the clinic. *Magn Reson Med*. 2018;80:507-520. doi:10.1002/mrm.27043
- Lawrenz M, Finsterbusch J. Detection of microscopic diffusion anisotropy in human cortical gray matter in vivo with double diffusion encoding. *Magn Reson Med*. 2019;81:1296-1306. doi:10.1002/mrm.27451
- Henriques RN, Palombo M, Jespersen SN, Shemesh N, Lundell H, Ianuş A. Double diffusion encoding and applications for biomedical imaging. *J Neurosci Methods*. 2021;348:108989. doi:10.1016/j.jneumeth.2020.108989
- Berry DB, Galinsky VL, Hutchinson EB, Galons JP, Ward SR, Frank LR. Double pulsed field gradient diffusion MRI to assess skeletal muscle microstructure. *Magn Reson Med*. 2023;90:1582-1593. doi:10.1002/mrm.29751
- Jespersen SN. Equivalence of double and single wave vector diffusion contrast at low diffusion weighting. *NMR Biomed*. 2012;25:813-818. doi:10.1002/nbm.1808
- Jespersen SN, Lundell H, Sonderby CK, Dyrby TB. Orientationally invariant metrics of apparent compartment eccentricity from double pulsed field gradient diffusion experiments. *NMR Biomed*. 2013;26:1647-1662. doi:10.1002/nbm.2999
- Henriques RN, Jespersen SN, Shemesh N. Correlation tensor magnetic resonance imaging. *Neuroimage*. 2020;211:116605. doi:10.1016/j.neuroimage.2020.116605
- Beach TG, Adler CH, Sue LI, et al. Arizona study of aging and neurodegenerative disorders and brain and body donation program. *Neuropathology*. 2015;35:354-389. doi:10.1111/neup.12189
- Comrie CJ, Carlson R, Ahsan Z, et al. Identification of diffusion, kurtosis, and propagator MRI markers of Alzheimer's disease pathology in post-mortem human tissue. *Imaging Neuroscience*. 2024;2:1-19. doi:10.1162/imag_a_00164
- Serrano GE, Intorcia A, Carew J, et al. Feasibility study: comparison of frontal cortex needle core versus open biopsy

- for detection of characteristic proteinopathies of neurodegenerative diseases. *J Neuropathol Exp Neurol*. 2015;74:934-942. doi:10.1097/NEN.0000000000000235
29. Irfanoglu MO, Nayak A, Jenkins J, Pierpaoli C. Proceedings of the 25th Annual Meeting of ISMRM.TORTOISE v3: Improvements and New Features of the NIH Diffusion MRI Processing Pipeline. [Poster Session]. 25th Annual Meeting of the International Society for Magnetic Resonance. 2018. Paris, France.
 30. Jensen JH, Helpert JA. MRI quantification of non-Gaussian water diffusion by kurtosis analysis. *NMR Biomed*. 2010;23:698-710. doi:10.1002/nbm.1518
 31. Fieremans E, Jensen JH, Helpert JA. White matter characterization with diffusional kurtosis imaging. *Neuroimage*. 2011;58:177-188. doi:10.1016/j.neuroimage.2011.06.006
 32. Glenn GR, Helpert JA, Tabesh A, Jensen JH. Quantitative assessment of diffusional kurtosis anisotropy. *NMR Biomed*. 2015;28:448-459. doi:10.1002/nbm.3271
 33. Garyfallidis E, Brett M, Amirbekian B, et al. Dipy, a library for the analysis of diffusion MRI data. *Front Neuroinform*. 2014;8:8. doi:10.3389/fninf.2014.00008
 34. Avants B, Gee JC. Geodesic estimation for large deformation anatomical shape averaging and interpolation. *Neuroimage*. 2004;23:S139-S150. doi:10.1016/j.neuroimage.2004.07.010
 35. Schindelin J, Arganda-Carreras I, Frise E, et al. Fiji: an open-source platform for biological-image analysis. *Nat Methods*. 2012;9:676-682. doi:10.1038/nmeth.2019
 36. Shepherd TM, Özarslan E, King MA, Mareci TH, Blackband SJ. Structural insights from high-resolution diffusion tensor imaging and tractography of the isolated rat hippocampus. *Neuroimage*. 2006;32:1499-1509. doi:10.1016/j.neuroimage.2006.04.210
 37. Zeineh MM, Palomero-Gallagher N, Axer M, et al. Direct visualization and mapping of the spatial course of fiber tracts at microscopic resolution in the human hippocampus. *Cereb Cortex*. 2017;27:1779-1794. doi:10.1093/cercor/bhw010
 38. Calabrese E, Hickey P, Hulette C, et al. Postmortem diffusion MRI of the human brainstem and thalamus for deep brain stimulator electrode localization. *Hum Brain Mapp*. 2015;36:3167-3178. doi:10.1002/hbm.22836
 39. Prats-Galino A, Soria G, de Notaris M, Puig J, Pedraza S. Functional anatomy of subcortical circuits issuing from or integrating at the human brainstem. *Clin Neurophysiol*. 2012;123:4-12. doi:10.1016/j.clinph.2011.06.035
 40. Amaral DG, Scharfman HE, Lavenex P. The dentate gyrus: fundamental neuroanatomical organization (dentate gyrus for dummies). *Prog Brain Res*. 2007;163:3-22. doi:10.1016/S0079-6123(07)63001-5
 41. Naidich TP, Duvernoy HM, Delman BN, Sorensen AG. *Duvernoy's Atlas of the Human Brain Stem and Cerebellum: High-Field MRI, Surface Anatomy, Internal Structure, Vascularization and 3D Sectional Anatomy*. Springer; 2009.
 42. Braak H, Thal DR, Ghebremedhin E, Del Tredici K. Stages of the pathologic process in Alzheimer disease: age categories from 1 to 100 years. *J Neuropathol Exp Neurol*. 2011;70:960-969. doi:10.1097/NEN.0b013e318232a379
 43. Balls GT, Frank LR. A simulation environment for diffusion weighted MR experiments in complex media. *Magn Reson Med*. 2009;62:771-778. doi:10.1002/mrm.22033
 44. Baxter GT, Frank LR. A computational model for diffusion weighted imaging of myelinated white matter. *Neuroimage*. 2013;75:204-212. doi:10.1016/j.neuroimage.2013.02.076
 45. Hutchinson EB, Avram AV, Irfanoglu MO, et al. Analysis of the effects of noise, DWI sampling, and value of assumed parameters in diffusion MRI models. *Magn Reson Med*. 2017;78:1767-1780. doi:10.1002/mrm.26575
 46. Komlos ME, Benjamini D, Hutchinson EB. Using double pulsed-field gradient MRI to study tissue microstructure in traumatic brain injury (TBI). *Microporous Mesoporous Mater*. 2017;269:156-159.
 47. Benjamini D, Hutchinson EB, Komlos ME, et al. Direct and specific assessment of axonal injury and spinal cord microenvironments using diffusion correlation imaging. *Neuroimage*. 2020;221:117195. doi:10.1016/j.neuroimage.2020.117195

SUPPORTING INFORMATION

Additional supporting information may be found in the online version of the article at the publisher's website.

Figure S1. The correlation tensor imaging (CTI) metric map of K_{aniso} was compared with the diffusion tensor subspace imaging (DiTSI) metric map spherical anisotropy (SA) including by composite mapping, in which K_{aniso} is overlaid on the SA map using a red colorscale. Both frameworks used cubic-encoded data. Small fascicles (*magenta arrows*) were only observed by SA, and the K_{aniso} maps were strongly positive in only a subset of high anisotropy regions.

Figure S2. The single diffusion encoding (SDE) anisotropy metric maps of propagator anisotropy (PA) and diffusion kurtosis imaging (DKI)-microscale anisotropy (μA) and the double diffusion encoding (DDE) correlation tensor imaging (CTI) metric map of K_{aniso} were compared with the DiTSI metric map SA, including by composite mapping, in which the SA map used the green channel and other maps used the red channel. Both DDE frameworks used dodecahedral encoding. High anisotropy regions were notably nonoverlapping between the metrics.

How to cite this article: Hutchinson EB, Galons J-P, Comrie CJ, et al. Diffusion tensor subspace imaging of double diffusion-encoded MRI delineates small fibers and gray-matter microstructure not visible with single encoding techniques. *Magn Reson Med*. 2025;93:2370-2385. doi: 10.1002/mrm.30463